Géotechnique **00**, 1–23 [http://dx.doi.org/10.1680/geot.XX.XXXXX]

Continuum solutions for tunnel-building interaction and a modified framework for deformation prediction

A. FRANZA*, S. RITTER† and M. J. DEJONG‡

In this paper, the response of buildings to tunnelling-induced ground movements is studied with elastic and elastoplastic continuum solutions that consider the structure as an equivalent simple beam. A comparison is made between these simple solutions and centrifuge test data to provide insights into flexural and axial building deformations of low-rise bearing wall structures on strip foundations; the influence of wall openings and the foundation scheme on the equivalent beam bending stiffness is also addressed. Subsequently, the effects of structural continuity across greenfield sagging and hogging regions on tunnel-structure interaction are investigated. Finally, the continuum solutions are used to propose a modification factor formulation that accounts for the change in settlement trough shape (compared to the greenfield) due to soil-structure interaction. This formulation, for example, accounts for the change in transverse length of the hogging and sagging regions of a building due to soil-structure interaction, eliminating the need to divide the building at the greenfield inflection points when calculating modification factors. The proposed formulation, which is compared with numerical, experimental and field data from previous research, is shown to better predict flexural building deformations.

KEYWORDS: Tunnels & tunnelling, settlement, soil/structure interaction, elasticity, centrifuge modelling

INTRODUCTION

The development of urban areas often requires the excavation of new tunnels; this process can affect surface buildings and infrastructure. Tunnelling-induced structure deformations depend on ground movements, structure stiffness, load condition, and structural configuration (both foundation and superstructure). In particular, the role of structure characteristics in tunnel-structure interaction (TSI) has been primarily investigated with numerical modelling and field data (Bilotta *et al.*, 2017; Dimmock & Mair, 2008; Farrell *et al.*, 2014; Franzius *et al.*, 2006; Giardina *et al.*, 2015; Fargnoli *et al.*, 2015; Losacco *et al.*, 2014; Mair, 2013; Pickhaver *et al.*, 2010), although centrifuge tests of TSI have also been performed (Farrell *et al.*, 2014; Franza & Marshall, 2018; Ritter *et al.*, 2017a,b; Taylor & Grant, 1998; Taylor & Yip, 2001).

This paper aims to illustrate, through comparison with centrifuge data, the efficiency of simple continuum solutions in predicting the tunnelling-induced deformations of low-rise bearing wall structures on strip foundations. Then, using these continuum solutions, the influence of structure continuity across sagging and hogging greenfield settlement regions on TSI is investigated. Finally, a modified framework for the estimation of flexural modification factors is proposed.

BACKGROUND

Greenfield tunnelling in soft soils

Tunnelling induces both vertical (u_z) and horizontal (u_x) ground movements at the surface. Greenfield tunnelling-induced ground movements are often assessed, as shown in Figure 1, with empirical methods based on Gaussian curves and the tunnel volume loss parameter ($V_{l,t}$), which is the ground loss at the tunnel periphery per unit length of tunnel normalised by the tunnel area.

Manuscript received...
* ETSI Caminos, Canales y Puertos, Technical University of Madrid, Madrid, Spain. Formerly, Department of Engineering, University of Cambridge, Cambridge, UK.
† Department of Engineering, University of Cambridge, Cambridge, UK.
‡ Department of Civil and Environmental Engineering, University of California, Berkeley, USA.

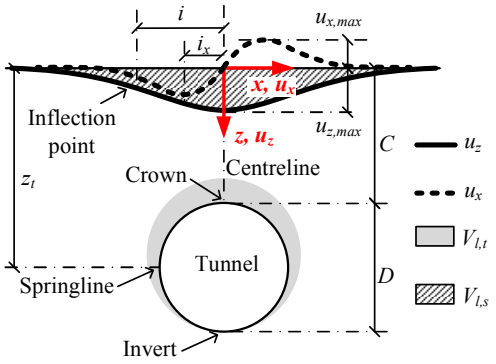

Fig. 1. Surface ground movements and volume losses.

In clays, surface settlement troughs are predicted with the use of standard Gaussian curves displayed in Equation (1) (Peck, 1969; Mair *et al.*, 1993).

$$u_z = u_{z,max} \exp\left(-\frac{x^2}{2i^2}\right) \tag{1}$$

where x is the horizontal spatial coordinate, $u_{z,max}$ is the maximum settlement, i is the horizontal distance of the settlement trough inflection point to the tunnel centreline, and z_t is the tunnel axis depth.

In sandy soils, modified Gaussian curves (Equation (2)) better replicate settlement troughs (Vorster *et al.*, 2005); trough width increases with C/D and decreases with $V_{l,t}$, whereas the dependence on the relative soil density varies with C/D (Franza *et al.*, 2018; Marshall *et al.*, 2012; Sugiyama *et al.*, 1999). For sandy soils, a good fit to surface u_x is achievable with Equation (3) (Farrell, 2010).

$$u_z = \frac{u_{z,max} \cdot n}{(n-1) + \exp\left[a\left(x/i\right)^2\right]}; n = e^a \frac{2a-1}{2a+1} + 1 \tag{2}$$

$$u_x = u_{x,max} \frac{1.65x}{i_x} \exp\left[-\frac{x^2}{2i_x^2}\right] \tag{3}$$

where n is the shape factor (if $n = 1$, Equation (2) is the standard Gaussian curve), a is the parameter to ensure that i remains the distance to the inflection point, and i_x is the horizontal offset of the maximum horizontal displacement, $u_{x,max}$.

Continuum solutions

The two-stage solutions proposed by Franza & DeJong (2018), incorporated into a computer program 'ASRE', were adopted in this paper. As shown in Figure 2, the surface structure is simulated by an Euler-Bernoulli elastic beam with no shear deformability and its axis located at the ground level. Structural loads are simulated by a distributed vertical load at the beam axis. The structure is connected to vertical and horizontal coupled springs that model the elastic homogeneous half-space continuum, the soil. As basic assumptions, the tunnel and structure presence does not influence, respectively, the response of the continuum and the tunnelling process. The cross-sectional properties and Young's modulus of the equivalent beam are chosen to represent the axial stiffness and bending stiffness of both the foundation and the superstructure combined. To allow for the separation and relative soil-structure sliding, perfectly plastic sliders are located between the soil springs and the structure. The tunnel-structure interaction (TSI) is solved, after applying vertical loads to the structure, by imposing surface greenfield movements to the springs in incremental steps.

The finite element method (FEM) is used to solve the TSI problem numerically, which is described by the following equilibrium equations

$$(\mathbf{S} + \mathbf{K}^*)\mathbf{u} = \mathbf{p} + \mathbf{K}^*(\mathbf{u}^{cat} + \mathbf{\Lambda}^* \left\langle (\mathbf{p} - \mathbf{S}\mathbf{u}) \right\rangle + \mathbf{u}^{sl}) \tag{4}$$

$$\left\langle (\mathbf{p} - \mathbf{S}\mathbf{u}) \right\rangle_i = f_{i,low} < (\mathbf{p} - \mathbf{S}\mathbf{u})_i < f_{i,up} \tag{5}$$

$$\left\langle (\mathbf{p} - \mathbf{S}\mathbf{u}) \right\rangle_j = |(\mathbf{p} - \mathbf{S}\mathbf{u})_j| < \mu(\mathbf{p} - \mathbf{S}\mathbf{u})_i \tag{6}$$

In Equations (4)-(6), $\mathbf{u}$ is the total structure displacement vector ($\mathbf{u}^T = [\mathbf{u}_i \quad \mathbf{u}_j \quad \mathbf{\Phi}_k]$, in which $\mathbf{u}_i$ and $\mathbf{u}_j$ consist of the translational displacements along z and x, respectively, whereas $\mathbf{\Phi}_k$ contains rotations of the finite element nodes), $\mathbf{u}^{cat}$ is the greenfield surface displacement due to tunnelling, $\mathbf{p}$ is the external loading vector of the structure, $\mathbf{S}$ is the structure

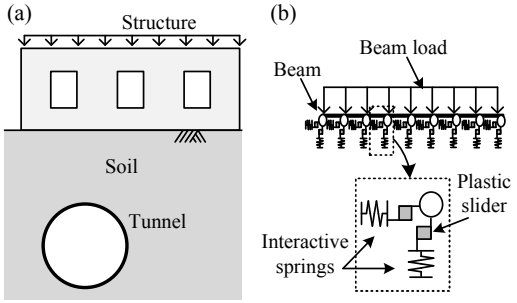

Fig. 2. (a) sketch of the problem; (b) mechanical representation of the model.

stiffness matrix, $\mathbf{\Lambda}$ is the soil flexibility matrix defined with the elastic integrated forms of Mindlin's solutions given by Vaziri *et al.* (1982), $\mathbf{\Lambda}^l$ is the local soil flexibility given by the diagonal matrix of $\mathbf{\Lambda}$, $\mathbf{\Lambda}^*$ is soil flexibility matrix without the main diagonal, $\mathbf{K}^* = (\mathbf{\Lambda}^l)^{-1}$ is the local stiffness matrix of the soil, $f_{i,up}$ and $f_{i,low}$ are the upper and lower limit loads of the vertical plastic sliders, and μ is the friction coefficient between the soil and foundation. In this study, $f_{i,low} = 0$ and $f_{i,up} = \infty$ (i.e. for vertical springs, linear elastic behaviour in compression and no tensile strength). The reaction forces applied by the soil to the foundation nodes are $\mathbf{F} = \mathbf{Su} - \mathbf{p}$, whereas the compatibility condition requires that the displacement vector $\mathbf{u} = \mathbf{u}^c + \mathbf{u}^{sl}$, in which $\mathbf{u}^c$ is the soil continuum displacements and $\mathbf{u}^{sl}$ is the slider displacements. An iterative and incremental procedure is needed to solve Equations (4)-(6) (Franza & DeJong, 2018).

A fully elastic method based on the perfect soil-structure bonding condition is obtained by imposing $\mathbf{u}^{sl} = 0$. In this case, Equation (4) can be written as Equation (7). Because of the superposition principle, tunnelling-induced displacements can be calculated assuming $\mathbf{p} = 0$.

$$(\mathbf{S} + \mathbf{K}^* + \mathbf{K}^*\mathbf{\Lambda}^*\mathbf{S})\mathbf{u} = \mathbf{p} + \mathbf{K}^*\mathbf{\Lambda}^*\mathbf{p} + \mathbf{K}^*\mathbf{u}^{cat} \tag{7}$$

In this study, purely elastic and elastoplastic solutions are referred to as 'EL' and 'EP', respectively.

Tunnelling-induced structure deformations and the role of soil-structure interaction

Tunnelling-induced structural damage is often assessed by assuming that the structure deforms according to the greenfield conditions. A maximum building tensile strain, ε_{max}, is then calculated with deep beam theory; ε_{max} depends on bending strain (ε_b), diagonal strain (ε_d), and average horizontal axial strain (ε_h) of the structure (Burland & Wroth, 1974; Boscardin & Cording, 1989; Mair *et al.*, 1996).

$$\varepsilon_b = \frac{DR}{\left(\frac{B_r}{12t} + \frac{3I}{2tB_rH}\frac{E}{G}\right)} \qquad \varepsilon_d = \frac{DR}{\left(1 + \frac{HB_r^2}{18I}\frac{G}{E}\right)} \tag{8}$$

where H is the height of the building, B_r is the building transverse length in the sagging or hogging region (indicated as $B_{sag,bld}$ and $B_{hog,bld}$, respectively, in Figure 3), E and G are the Young's and shear moduli, I is the second moment of area of the idealised beam, t is the maximum distance between the neutral axis and the edge of the beam in tension, and DR is the deflection ratio (defined in Figure 3). The structure transverse length and location with respect to the tunnel centreline can be defined in terms of D_u and D_l, which are discussed later in the text.

Stiff structures react to ground displacements and deform less than a fully-flexible structures. To quantify this soil-structure interaction (SSI), modification factors for the deflection ratio, $M^{DR,sag}$ an $M^{DR,hog}$, were proposed by Potts & Addenbrooke (1997) as follows

$$M^{DR,sag/hog} = \frac{DR_{sag/hog,bld}}{DR_{sag/hog,gf}} \tag{9}$$

where building deflection ratios are $DR_{sag,bld}$ and $DR_{hog,bld}$ (depending on the structure inflection point, i_{bld}), deflection ratios of the greenfield settlement trough are $DR_{sag,gf}$ and $DR_{hog,gf}$ (determined by the greenfield inflection point position, i).

Structures with continuous horizontal foundation elements have a significant axial stiffness and, consequently, tunnelling-induced structural horizontal strains ε_h are generally low (Burland *et al.*, 2004; Dimmock & Mair, 2008). Similar to the DRs, Potts & Addenbrooke (1997) proposed that the modification factors for the average horizontal strain can be defined

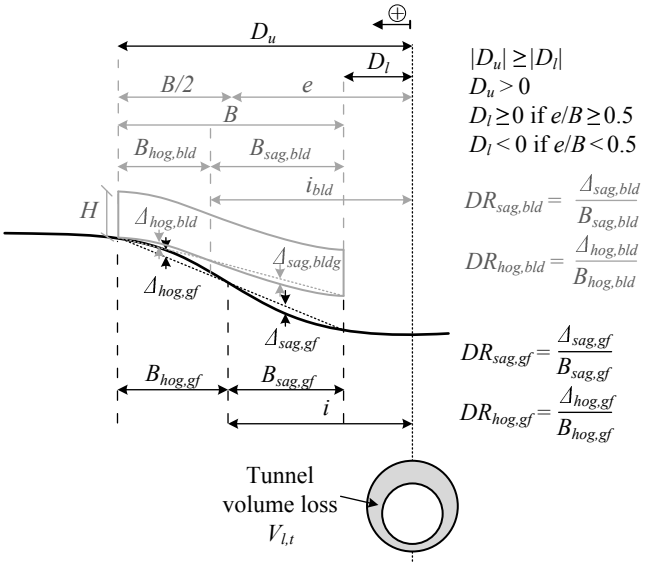

Fig. 3. Nomenclature for the flexural TSI problem.

as follows

$$M^{\varepsilon h,sag/hog} = \frac{\varepsilon_{h,sag/hog,bld}}{\varepsilon_{h,sag/hog,gf}} \tag{10}$$

where $\varepsilon_{h,sag/hog,bld}$ and $\varepsilon_{h,sag/hog,gf}$ are computed, respectively, within $B_{sag/hog,bld}$ and $B_{sag/hog,gf}$.

Methods based on the relative structure-soil stiffness have been proposed to assess M^{DR}. For example, Franzius *et al.* (2006) and Mair (2013) defined, respectively, ρ^*_{mod} and ρ_{sag}, ρ_{hog} as dimensionless relative stiffness factors that are expressed as

$$\rho^*_{mod} = \frac{EI}{E_s z_t B^2 L} = \frac{EI^*}{E_s z_t B^2} \tag{11}$$

$$\rho_{sag/hog} = \frac{EI}{E_s B^3_{sag/hog,gf} L} = \frac{EI^*}{E_s B^3_{sag/hog,gf}} \tag{12}$$

where EI is the bending stiffness of the superstructure (in kN m^2), EI^* is EI per running metre (in kN m^2/m), E_s is a soil Young's modulus representative of the soil affected by the excavation (accounting for the average elastic modulus of the soil above the tunnel and the soil stiffness degradation with strain level), L is the longitudinal length of the building in the tunnel axis direction, $B_{sag,gf}$ and $B_{hog,gf}$ are the transverse lengths of the building in the sagging and hogging zones based on the greenfield settlement trough.

Franzius *et al.* (2006) and Mair (2013) proposed design charts in which M^{DR} are related to ρ^*_{mod} and ρ_{sag}, ρ_{hog}, respectively. Franzius *et al.* (2006) envelopes vary with the normalised tunnel-structure eccentricity e/B (see Figure 3) and deformation zone. However, ρ^*_{mod} does not account for the shape of the greenfield settlement trough that is related to i, although Franzius *et al.* (2006) results displayed that, for a given structure, M^{DR} increases with tunnel depth z_t (thus i).

Mair (2013) proposed ρ_{sag} and ρ_{hog} and the same design relationship $M^{DR} - \rho$ in sagging and hogging zones. In addition, $B_{sag,gf}$ and $B_{hog,gf}$ relate to i and thus ρ_{sag} and ρ_{hog} indirectly account for the shape of the settlement trough (consequently, ρ_{sag} and ρ_{hog} could be used for both tunnelling in clays and sands). The definition of ρ_{sag} and ρ_{hog} implies that a structure spanning both hogging and sagging zones responds to tunnelling as independent structures in each deformation zone. However, structural stiffness can modify the shape of the building settlement curve; consequently, the locations of the inflection points of the structure (i_{bld}) and the greenfield settlement trough (i) may differ, as shown in Figure 3 (Farrell *et al.*, 2014; Frischmann *et al.*, 1994; Lu *et al.*, 2001; Potts & Addenbrooke, 1997; Taylor & Yip, 2001).

Equation (12) was modified by Giardina *et al.* (2015) to account for the structure weight effects on M^{DR}; however, Bilotta *et al.* (2017), Franzius *et al.* (2004), Giardina *et al.* (2015), and Franza & DeJong (2018) concluded that the influence of the self-weight on M^{DR}, while important in some cases, is generally secondary compared to the role of bending stiffness for ordinary structures and low-medium volume losses.

Finally, as displayed by Equation (8), tensile strains depend on the building transverse length $B_r = B_{sag,bld}$ or $B_{hog,bld}$. Therefore, assuming $B_{sag/hog,bld} = B_{sag/hog,gf}$ (implying $i_{bld} = i$) can lead to erroneous damage assessment. To account for the variation in shape of the building settlement curve, the modification factors $M^{B,sag}$ and $M^{B,hog}$ for the sagging and

hogging region length are defined as follows

$$M^{B,sag/hog} = \frac{B_{sag/hog,bld}}{B_{sag/hog,gf}} \tag{13}$$

M^B has received less attention in the literature than M^{DR}. Farrell (2010) suggested an empirical correlation between i_{bld}/i and structure-soil stiffness, whereas Potts & Addenbrooke (1997) and Franza *et al.* (2017) suggested that structure deflection shape is dependent on shear deformability and structural configuration, respectively, which are related.

COMPARISON OF CONTINUUM SOLUTION PREDICTIONS WITH CENTRIFUGE DATA

Results from the centrifuge test series performed by Ritter *et al.* (2017a,b) at $75g$ were considered. In the following, both model dimensions and results are reported in prototype scale. 1/75th scale models, each consisting of a bearing wall structure with openings on strip footings affected by tunnelling, were tested (see Figure 4). The tunnel was excavated in uniform dense dry silica sand (soil relative density $I_d = 90\%$) and simulated with a plane-strain model tunnel. At prototype scale, a 6.2m diameter (D) tunnel with a cover-to-diameter ratio $C/D = 1.3$ and a depth to tunnel axis $z_t = 11.3$m was modelled. The model structure was obtained through 3D printing of a material with properties similar to masonry. The structure was orthogonal to the tunnel. The opening ratio, O, of the transverse walls (simulating window distributions) ranged between 20% and 40%. Only external walls were supported by strip footings (see Figure 4(b)); this structural detail is taken into account in this paper considering the ratio χ between the soil-foundation contact surface A_f (i.e. the area of the footing) and the area of the building $A_s = B \times L$. Model structures were located both centrally and eccentrically with respect to the tunnel centreline (corresponding to $x = 0$) with a normalised eccentricity e/B varying between 0 and 0.8. The average stress at the contact area between strip footings, A_f, and soil was $\sigma = 80$kPa.

EI and EA of the entire structure were estimated as the summation of the contributions of the walls and foundation elements in the transverse direction to the tunnel axis (see dashed lines in Figure 4(c)); computed EI and EA values are reported in Table 1, normalised by the longitudinal structure length L. The second moment of area I of each element was taken relative to the structure neutral axis for pure bending deformations (e.g. the geometric centroid of the full cross-section composed of wall and foundation for a uniform material). In the following, the term 'neutral axis' is used to indicate the axis where the longitudinal strain is zero for pure bending deformations; however, there can be longitudinal strains at the 'neutral axis' due to axial deformations. To account for the openings, EI and EA of the bearing walls were computed by decreasing the cross-section values, respectively, by the reduction factor α given by Melis & Rodriguez Ortiz (2001) and λ, which is the ratio between average cross-sectional area over the building transverse length B and full cross-section area. For $O = 20$ and 40%, $\alpha = 0.60, 0.15$ whereas $\lambda = 0.80, 0.60$, respectively. The stiffening effect of transverse walls was neglected because the main structural deflection is obtained in the transverse plane. It should be also noted that α and λ do not account for the effects of the opening shape and their distribution.

Previous research mostly investigated the TSI by adopting equivalent beam and plate models of the structure (Potts & Addenbrooke, 1997; Franzius *et al.*, 2006; Farrell *et al.*, 2014; Namazi & Mohamad, 2013a). These equivalent models are fully representative for buildings with a raft foundation because the entire equivalent structure is in contact and interacts with the underlying soil; consequently, $EI^* = EI/L$ and $EA^* = EA/L$ are well defined for raft foundations. However, average stiffness values (EI/L, EA/L) reported in Table 1 neglect that in the centrifuge tests the foundation consists of strip footings and that, consequently, only the soil directly beneath the foundation elements is interacting with the structure. To incorporate this foundation scheme, bending and axial stiffness per metre run (EI^*, EA^*) are estimated as follows

$$EI^* = \frac{EI}{\chi L}\ [\text{kNm}^2/\text{m}] \qquad EA^* = \frac{EA}{\chi L}\ [\text{kN/m}] \tag{14}$$

where $\chi = 1$ for raft foundations and $\chi = A_f/A_s \leq 1$ for strip and separated footings (see Figure 4(b)). However, this approximation has limitations because it does not account for the shape of the 3D foundation scheme and the location of the footings with respect to the tunnel axis.

Finally, it should be noted that for the considered buildings on continuous strip footings, $EI^* = EI_{facade}/d_{foot}$ could have been an alternative approach, where EI_{facade} is the facade stiffness and d_{foot} is the footing cross-sectional width in the longitudinal direction. However, for the centrifuge buildings, this approach neglects the presence of the longitudinal footings and would overestimate the structure stiffness with respect to the soil.

For the elastic continuum, a Young's modulus $E_s = 45$MPa and a Poisson's ratio $\nu_s = 0.25$ were assumed; this E_s value represents a lower bound estimation for the simulated soil conditions at $V_{l,t} \leq 2\%$ (Ritter, 2017). The friction coefficient μ

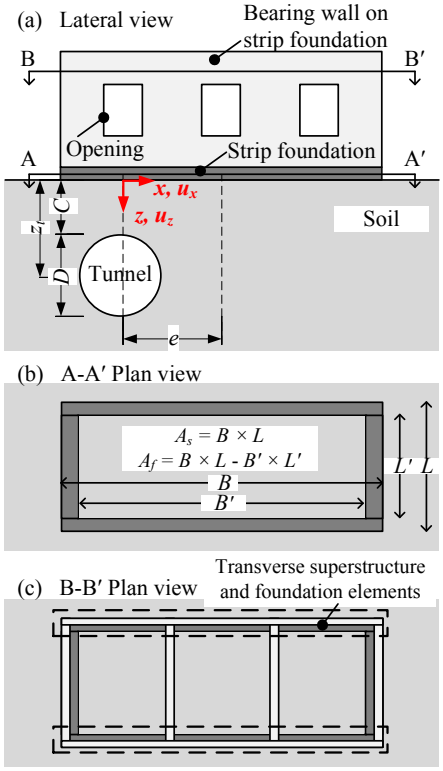

Fig. 4. Configuration modelled in centrifuge tests.

Table 1. Centrifuge test series of TSI (in prototype scale).

Label Test	B (m)	e/B (-)	O (%)	EA/L† (kN/m)	EI/L† (kNm)	χ (-)
SR-A	15.0	0	20	4.5 10^5	1.5 10^6	0.30
SR-B	15.0	0.8	20	4.0 10^5	1.3 10^6	0.30
SR-C	15.0	0.5	20	3.7 10^5	1.2 10^6	0.30
SR-D	15.0	0.8	40	2.0 10^5	4.0 10^5	0.30
SR-E	19.5	0.5	20	3.5 10^5	1.1 10^6	0.28
SR-F	19.5	0.5	40	4.1 10^5	8.1 10^5	0.28
$L = 7.5$m; $\sigma = 80$kPa						
† Considering openings in walls						

between the foundation and the continuum was specified to be $\tan(30°)$. The input displacement vector $\mathbf{u}^{cat}$ was defined on the basis of the greenfield centrifuge test from Marshall *et al.* (2012) by curve-fitting surface measurements of soil u_z and u_x with Equations (2) and (3).

The characteristics of the implemented equivalent simple beams are reported in Table 2. The subscript m was added to indicate the properties of the equivalent beam model. The equivalent beams had a finite element size of 0.5m and a transverse length matching the corresponding prototype structure B. The Young's moduli, E_m, and cross-sectional dimensions (depth, $d_{b,m}$, and width, $b_{b,m} = 1$m) of the equivalent simple beams were set to match the cross-sectional properties $E_m I^*_m$ and $E_m A^*_m$ with the prototype EI^* and EA^* of the centrifuge model buildings ($E_m A^*_m = EA^*$, $E_m I^*_m = EI^*$). Two equivalent simple beams with varying cross-sectional properties were adopted for a given centrifuge test to investigate the influence of the ratio χ of the target building in TSI analyses. As shown in Table 2, two simulation series, labelled 'SRs' and 'SRf', were carried out with ($E_m I^*_m/1$, $E_m A^*_m/1$) equal to (EI/L,EA/L) and ($EI/(\chi L)$,$EA/(\chi L)$), respectively. Finally, a uniform vertical load $q_{z,m} = \sigma \times b_{b,m} = 80$kN/m was adopted.

Firstly, tunnelling-induced vertical displacements (u_z) of equivalent beams SRf, predicted by the elastic EL (black dashed lines) and elastoplastic EP (black solid lines) solutions, are compared with the centrifuge measurements in Figures 5 and 6 for $V_{l,t} = 1, 2\%$. Note that centrifuge displacements are reported both at the foundation level ($z = 0$ indicated as z_g) and at the height of the neutral axis of the structure ($z = -2.5$m indicated as z_b), which was computed considering the strip foundation and the bearing wall as a composite beam. Furthermore, plastic slider displacements from EP solutions (black markers) as well as contact stresses σ between the equivalent beam and the soil (grey lines) are plotted. Greenfield settlements are

Table 2. Equivalent simple beams.

Label	B_m (m)	$d_{b,m}$ (m)	E_m (Pa)	Target	$E_m I_m/1$, $E_m A_m/1$
SRs-A	15	6.3	$7.1\ 10^7$	SR-A	EI/L,
SRs-B	15	6.2	$6.5\ 10^7$	SR-B	EA/L
SRs-C	15	6.3	$5.8\ 10^7$	SR-C	
SRs-D	15	4.9	$4.2\ 10^7$	SR-D	
SRs-E	19.5	6.2	$5.6\ 10^7$	SR-E	
SRs-F	19.5	4.9	$8.3\ 10^7$	SR-F	
SRf-A	15	6.3	$2.4\ 10^8$	SR-A	$EI/(\chi L)$,
SRf-B	15	6.2	$2.2\ 10^8$	SR-B	$EA/(\chi L)$
SRf-C	15	6.3	$2.0\ 10^8$	SR-C	
SRf-D	15	4.9	$1.4\ 10^8$	SR-D	
SRf-E	19.5	6.2	$2.0\ 10^8$	SR-E	
SRf-F	19.5	4.9	$3.0\ 10^8$	SR-F	
$b_{b,m=}$1m; $q_z = 80$kN/m					

also displayed (dotted lines). Finally, acronyms are used in the legend: STR for the structure; SLD for the slider; EXP for experimental results.

Regarding centrifuge test outcomes, settlement data at the two heights z_g and z_b are nearly identical (the difference is within the error in the experimental measurement). In addition, the eccentric structures with $e/B > 0$ in Figures 5(b)-(f) and 6(b)-(f) displayed a semi-flexible response and greater settlements than greenfield curves, particularly at high volume losses; this is in agreement with numerical analyses performed in previous works (Bilotta *et al.*, 2017; Burd *et al.*, 2000; Franzius *et al.*, 2004). Meanwhile, the central structure SR-A with $e/B = 0$ in Figure 6(a) underwent small deflections with respect to greenfield curves.

Although EL and EP solutions cannot capture the increased level of settlements due to the structure weight, they generally match the structure deflections from the centrifuge tests reasonably well. Additionally, the EL and EP solutions are identical for all structures except for SRf-A in Figure 6(a), for which EP predicted u^{sl} greater than zero (this agrees with centrifuge tests: gap formation occurred above $V_{l,t} \approx 1.5\%$); in the other scenarios, the beam stiffness was not sufficiently stiff to result in the complete unloading of the soil. This statement is supported by the plot of the contact stresses σ, which reach null values over a significant transverse length only in Figures 5(a) and 6(a).

Finally, the variation in the soil-beam contact stress profile (σ), which is due to tunnelling-induced load redistribution along the structure, is considered in order to provide further insights into TSI. The stress results in Figures 6(a), (b) and (c) (structures with the same transverse length B and opening percentage O) show that [i] load redistribution varied with e/B, which indicates a different SSI mechanism, and [ii] increased e/B reduced the magnitude of the load redistribution.

In Figures 7 and 8, horizontal greenfield and structure displacement profiles (u_x) are displayed with a layout consistent to Figures 5 and 6; slider displacements are indicative of beam-soil slippage rather than gap formation. For SR-F visible cracking occurred at $V_{l,t} = 2.6\%$ (Ritter, 2017) and potential micro-cracking might have occurred at even lower volume loss values (see Figures 6(f) and 8(f)), whereas cracking started at a greater $V_{l,t}$ in the other tests. Consequently, material nonlinearity should be relatively insignificant for the volume loss range of interest.

Although tunnel engineers often measure structure axial deformations with monitoring systems placed near the ground level, experimental data show qualitative differences between structure displacements u_x at the ground level, z_g, and the neutral axis height, z_b (compare light and dark markers). In particular, these displacement profiles are associated with different horizontal strains $\varepsilon_h = u'_x(x,z)$ (i.e. $u'_x(x,z_g) \neq u'_x(x,z_b)$). Considering that [i] shear deformations do not result in ε_h and [ii] tilting effects on ε_h (due to the projection of the vertical self-weight along the tilted structure axis) are negligible for the modelled buildings (Namazi & Mohamad, 2013b), the variation in ε_h at the structure bottom z_g with respect to the level z_b was due the bending deformations. For instance, centrifuge data in Figure 8(e) show shortening of the structure fibres at z_g with respect to z_b level data. Consequently, when possible (e.g. during experimental testing), horizontal strain ε_h should be measured at the height of the structure's neutral axis.

Centrifuge data of structures with $e/B > 0$ shown in Figures 7(b)-(f) and 8(b)-(f) indicate that the structure is significantly dragged towards the tunnel centreline while horizontal strains tend to remain small and tensile (except in sub-plot(c)). On the other hand, the central structure SR-A with $e/B = 0$ was compressed by horizontal soil movements caused by tunnelling, and experienced negligible average u_x because of symmetry.

Taking into consideration the influence of bending on u_x, the EP predictions are compared in terms of overall shift (i.e. average displacements u_x over the building transverse length B) with the centrifuge u_x at the ground level z_g, whereas the horizontal strain level of the equivalent beam are compared with experimental ε_h at z_b. SRf beams (accounting for

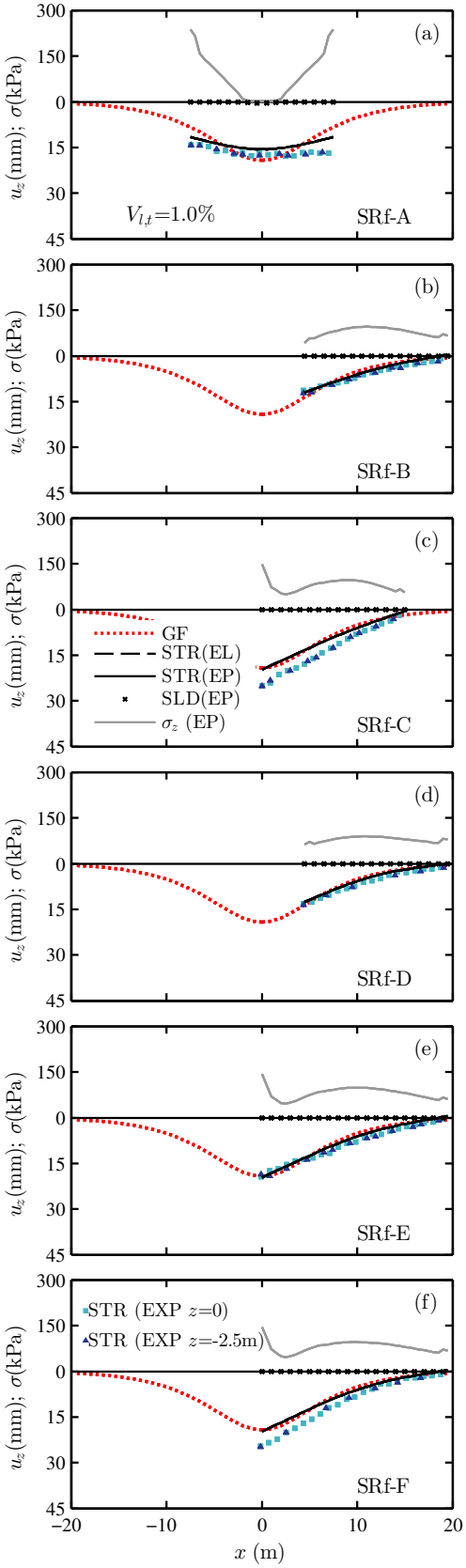

Fig. 5. Settlements of the building and in greenfield conditions as well as gap formation and contact stresses between the beam and the soil for $V_{l,t} = 1\%$.

199 the ratio χ) provide a good prediction of horizontal displacements and strains compared with centrifuge tests, except for
200 SR-C in Figures 7(c) and 8(c). During test SR-C, the bearing wall underwent significant axial compression above the tunnel

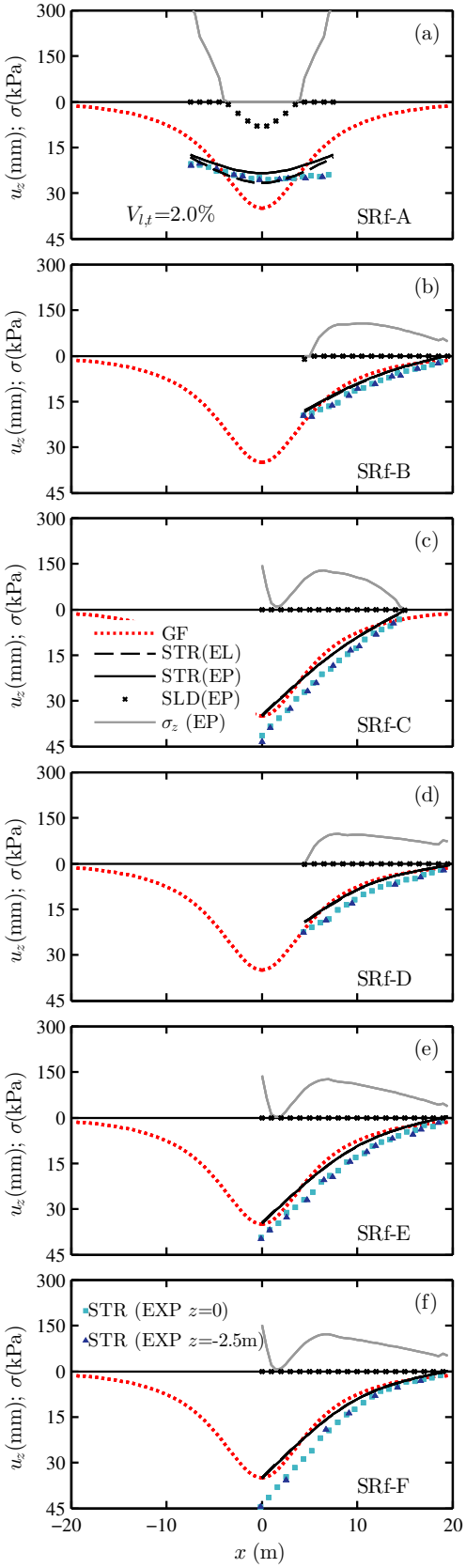

Fig. 6. Settlements of the building and in greenfield conditions as well as gap formation and contact stresses between the beam and the soil for $V_{l,t} = 2\%$.

201 $(x = 0 - 5\text{m})$ which was due to structure foundation embedment within the soil at the structure corner above the tunnel.

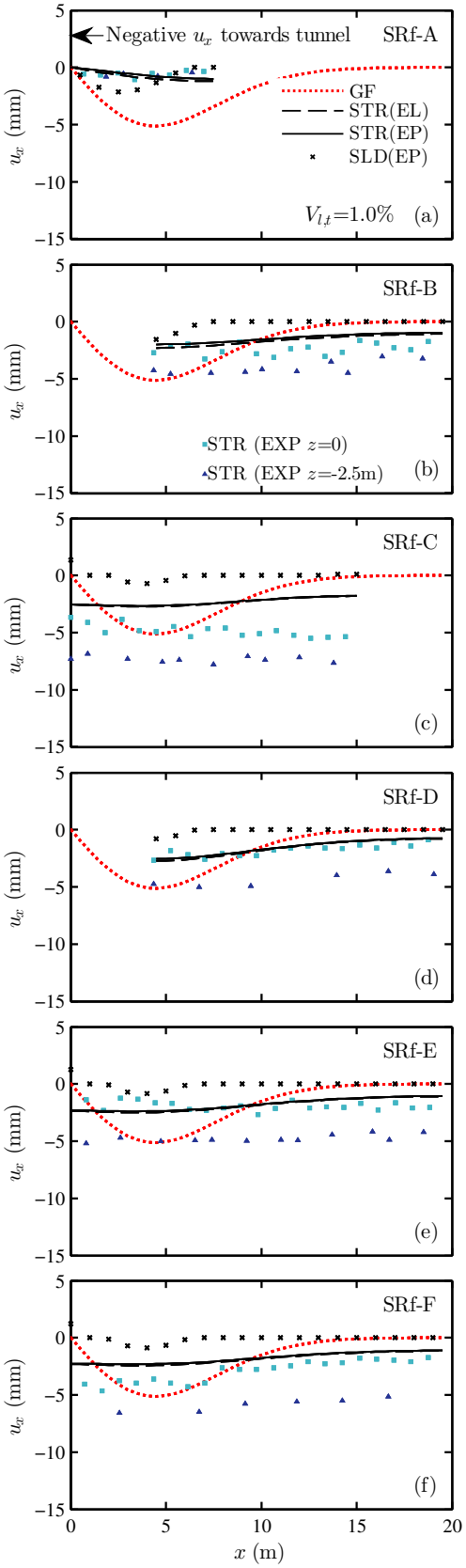

Fig. 7. Horizontal displacements of the building and in greenfield conditions as well as slippage between the beam and the soil for $V_{l,t} = 2\%$.

Finally, Figure 8 indicates that allowing for slippage in the EP solution resulted in lower axial strains with respect to the EL method, though the difference between the EP and EL results is relatively small.

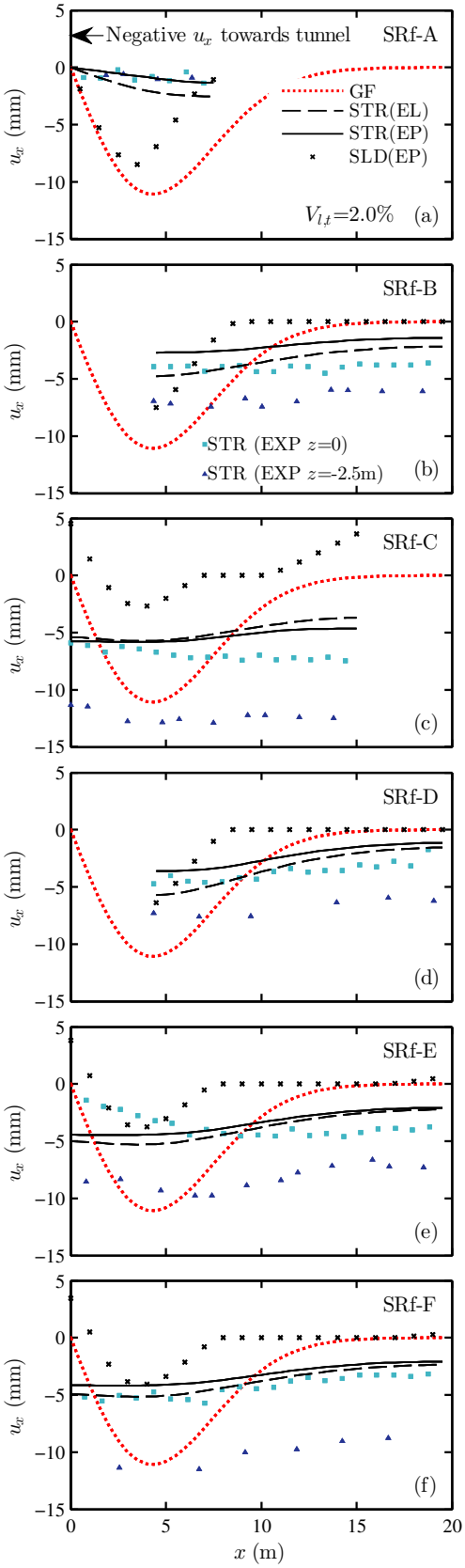

Fig. 8. Horizontal displacements of the building and in greenfield conditions as well as slippage between the beam and the soil for $V_{l,t} = 2\%$.

Next, modification factors for the deflection ratio (M^{DR}) and average horizontal strain ($M^{\varepsilon h}$) in the sagging and hogging regions for both centrifuge tests and EP solutions are shown in Figure 9. The plots provide information on the effects of χ by comparing continuum solutions for SRs and SRf structure (dashed and solid lines, respectively).

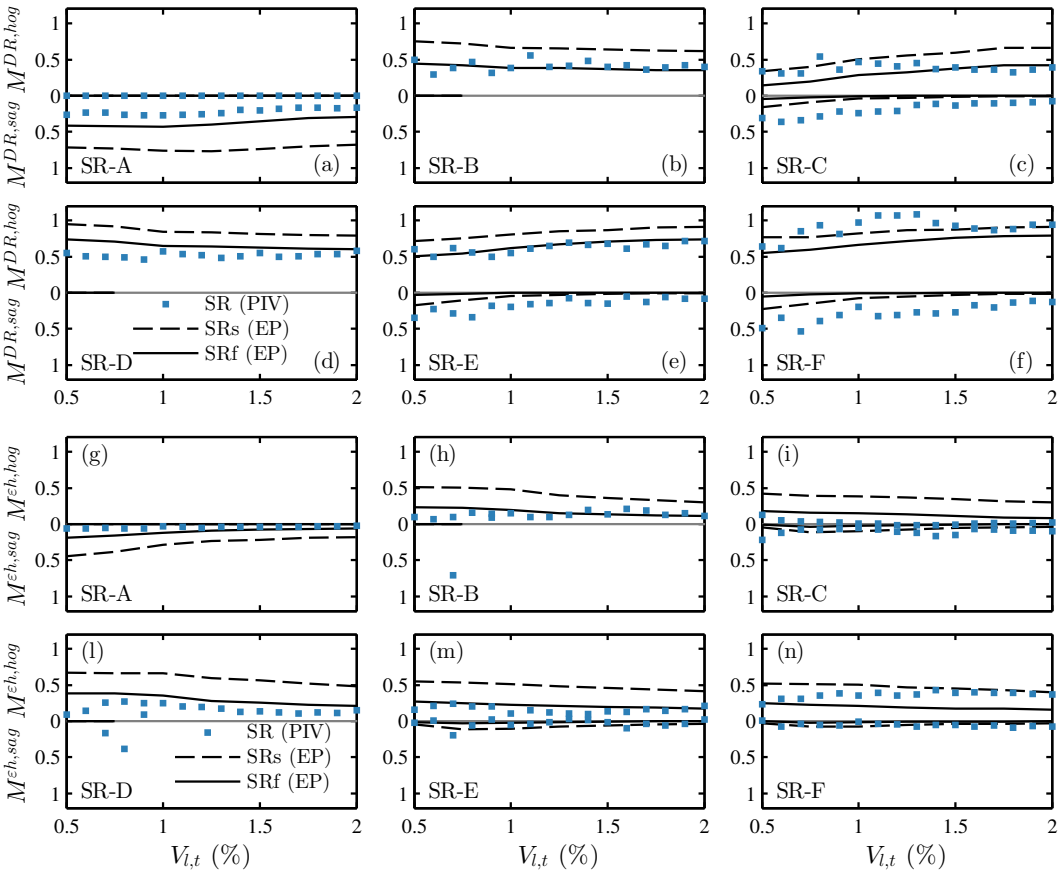

Fig. 9. Comparison between experimental and computed modification factor against $V_{l,t}$: (a)-(f) M^{DR}, (g)-(h) $M^{\varepsilon h}$.

Firstly, M^{DR} in Figures 9(a)-(f) are analysed. Solutions implementing SRf equivalent simple beams predicted $M^{DR,sag}$ for the central structure ($e/B = 0$) and $M^{DR,hog}$ for eccentric structures ($e/B \geq 0.5$) that are in good agreement with centrifuge data, except for the underestimation of hogging deformations of the longest structure SR-F in Figures 9(f). These errors were potentially due to the effects of the structure shear deformability. In addition, although SRf models slightly underestimated $M^{DR,sag}$ for $e/B \geq 0.5$ (Figures 9(b)-(f)), SRf beams captured that the response to tunnelling for eccentric building is more flexible in the hogging region than in the sagging zone (i.e. for $e/B \geq 0.5$, $M^{DR,hog} > M^{DR,sag}$). On the other hand, results in Figures 9(a)-(e) indicate that the use of simple beams SRs associated with $\chi = 1$ (dashed lines) resulted in the overestimation of $M^{DR,sag}$ and $M^{DR,hog}$ for central and eccentric buildings, respectively. Also note that adopting E_s higher than 45MPa (the adopted lower bound value) would result in M^{DR} values greater than shown in Figure 9. Thus, the results indicate that accounting for the ratio χ provides a more accurate prediction.

In Figures 9(g)-(n), EP solutions with SRf equivalent beams provided $M^{\varepsilon h}$ values in agreement with centrifuge results, except for the underestimation of $M^{\varepsilon h,hog}$ for SRf-F in Figure 9(n). Despite this, it should be noted that centrifuge structure SR-F had an average $\varepsilon_{h,hog}$ limited in magnitude (for instance, building $\varepsilon_{h,hog} < +0.03\%$ at $V_{l,t} = 2\%$); thus, the error resulting from the underestimation of $M^{\varepsilon h,hog}$ in Figure 9(n) in terms of structure tensile strains would be small. On the other hand, $M^{\varepsilon h}$ associated with SRs structures were greater than benchmark centrifuge data; thus, assuming EA^* from $\chi = 1$ underestimated relative structure-soil stiffness resulting in significant horizontal strains within the equivalent beam.

EFFECTS OF STRUCTURE CONTINUITY ACROSS SAGGING AND HOGGING GREENFIELD REGIONS

To investigate the effects of structure continuity (i.e. the interaction between the sagging and hogging portions of the structure) on the TSI mechanisms, structures with the same cross-sectional stiffness, but with different transverse length and eccentricity, were simulated. Greenfield ground movements and geotechnical parameters were assumed as in the previous section. A summary of the analysed scenarios is reported in Table 3. Structures ST-SS and ST-H were predominantly located in the sagging and hogging regions of the greenfield settlement trough, respectively. Structures ST-SSH and ST-HSSH were obtained by extending beams ST-SS in the hogging zone on one or both sides respectively, whereas the structures ST-SH

and ST-SSH are extended towards the sagging zone with respect to ST-H. The letters 'S' and 'H' indicate the sequence of sagging and hogging regions across the transverse length of the beam.

Table 3. Simple beams used to investigate structure continuity effects.

Label	B_m (m)	e/B (-)	$d_{b,m}$ (m)	E_m (Pa)
ST-SS	15	0	6.0	$2.0\ 10^8$
ST-SSH	27.5	0.23	6.0	$2.0\ 10^8$
ST-HSSH	40	0	6.0	$2.0\ 10^8$
ST-H	15	0.8	6.0	$2.0\ 10^8$
ST-SH	19.5	0.5	6.0	$2.0\ 10^8$
$b_{b,m} = 1$m; $q_z = 80$kN/m				

Settlements, u_z, of the simple beams in Table 3 predicted by EL and EP solutions are displayed in Figure 10. M^{DR} and B_r of the sagging and hogging deformation zones associated with greenfield curves and EL analyses are shown in Figures 11 and 12. Results in Figures 10(a), (b), (c) and 10(b), (d), (e) illustrate, respectively, the effects of the extension of structure towards the greenfield hogging and sagging region. In the following, the terms 'primary' and 'secondary' deformation modes are used as follows: for $e/B = 0 - 0.3$, primary = sagging and secondary = hogging; for $e/B \geq 0.5$, primary = hogging and secondary = sagging.

Firstly, the interaction mechanisms associated with structures ST-SS/SSH/HSSH are analysed, for which sagging is the primary deformation mode. Settlements in Figures 10(a), (b) and (c) display that, for structures with $e/B = 0 - 0.3$, the additional transverse length $B_{hog,gf}$ of the structure in the greenfield hogging region slightly decreased structure settlements because of the constraint given by the soil undergoing low tunnelling-induced settlements (at $x > 10$m). This is confirmed by the observed stress redistribution. Then, comparing greenfield settlement troughs and building displacements for ST-SSH and ST-HSSH in Figures 10(b) and (c), structural stiffness resulted in $i_{bld} > i$; consequently, the structure transverse length of sagging deflection, $B_{sag,bld}$, was greater than the greenfield value, $B_{sag,gf}$ (as confirmed by data in Figure 11(b)). In addition, the $M^{DR,sag}$ values shown in Figure 11(a) were significantly affected by the extension of the structure into the greenfield hogging region. Larger values of $B_{sag,bld}$ in Figure 11(b) correspond to an increase in $M^{DR,sag}$. For structures primarily in sagging, the increase in the structure transverse length in the greenfield hogging zone ($B_{hog,gf}$) decreased the relative structure-soil stiffness for sagging distortions and induced larger $M^{DR,sag}$. This interaction mechanism is not accounted for in Equation (12). Furthermore, the fact that $B_{hog,bld} < B_{hog}$ in Figure 11(b) for ST-SSH/HSSH indicates that the stiffness of the structure was sufficient to decrease the building hogging transverse length.

Next, the interaction mechanisms of structures ST-H/SH/SSH are addressed. Figure 10(e) displays that ST-SH ($e/B = 0.5$, hogging is the primary deformation mode) undergoes mostly hogging deformations despite a mixed sagging-hogging greenfield settlement trough (in Figure 12(b), $B_{sag,bld} = 0$ for $V_{l,t} > 1\%$). In addition, as shown in Figures 12(a), structure ST-SH was efficient in reducing the sagging distortions ($M^{DR,sag} = 0$), whereas the $M^{DR,hog}$ of this structure is greater than $M^{DR,hog}$ of ST-H. Note that the greenfield $B_{hog,gf}$ of ST-H and ST-SH are identical. The continuity of the structure across the greenfield inflection point clearly has a significant effect. In addition, the trends of $B_{sag,bld}/B_{hog,bld}$ and M^{DR} against $V_{l,t}$ in Figures 11 and 12 are due to the variation in the shape of the greenfield settlement curves with volume loss. Finally, the increase of the sagging transverse length between ST-SH and ST-SSH resulted in a structural behaviour mode dominated by the sagging deformations rather than the hogging deflection (see Figure 12).

These results illustrate that a continuous simple beam does not respond to the sagging and hogging portions of the greenfield settlement trough as independent sub-structures; TSI mechanisms due to structural continuity of simple beams [i] resulted in differences between $B_{sag,bld}/B_{hog,bld}$ and $B_{sag,gf}/B_{hog,gf}$, [ii] affected modification factors M^{DR}, and [iii] differed for structures with primary sagging ($e/B = 0 - 0.3$) and primary hogging ($e/B > 0.5$) deformation modes.

A MODIFICATION FACTOR BASED APPROACH

In this section, the EL analysis method is adopted to study $M^{DR,sag}$, $M^{DR,hog}$, $M^{B,sag}$, $M^{B,hog}$, which are referred to as 'flexural interaction parameters'. The influence of the weight of the structure on these parameters is neglected.

In the EL solution, by neglecting the horizontal greenfield movements and assuming that the greenfield settlement trough is given by a standard Gaussian curve (for both greenfield movements in clays and sands), the flexural interaction parameters depend on E_s, ν_s, i, EI^*, which have previously been defined, and D_u and D_l, which are maximum and minimum absolute offsets of the structure edges from the tunnel centreline, respectively, as shown in Figure 3. Note that $D_u > 0$ by definition, whereas $D_l < 0$ and $D_l > 0$ indicate that $e/B < 0.5$ and $e/B > 0.5$, respectively. If the influence of ν_s is neglected as

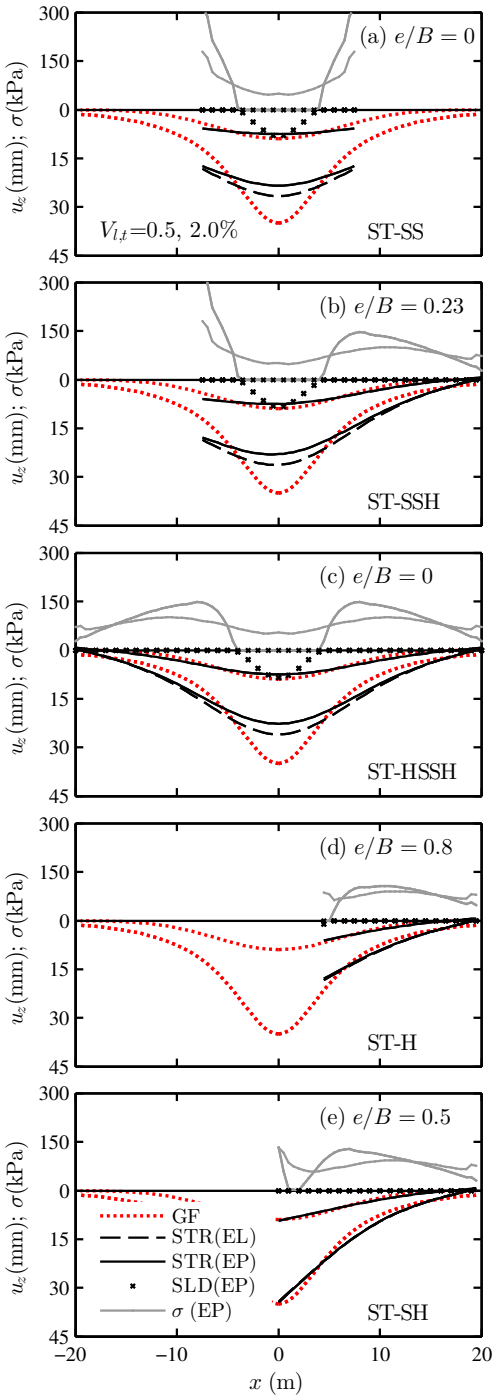

Fig. 10. Tunnelling-induced displacements and contact stress distributions: the effects of structure continuity.

discussed later, the flexural interaction parameters can be reduced to the following dimensionless groups

$$R = \frac{EI^*}{E_s i^3}, \qquad \frac{D_u}{i}, \qquad \frac{D_l}{i} \tag{15}$$

where R is the rigidity factor (Klar *et al.*, 2005).

In this section, analyses were performed for varying stiffness values of the simple beam (see Table 4) and $L = 1$m. Assuming $L = 1$m gives greater M^{DR} compared to higher L values or plane-strain conditions (Franzius *et al.*, 2006). Additional analyses were performed to investigate the effects of ν_s on TSI. The sensitivity of flexural interaction parameters to Poisson's ratio was minor and M^{DR} values associated with $\nu_s = 0.25$ were lower than for $\nu_s = 0.5$. In particular, the difference in M^{DR} between $\nu_s = 0.5$ and 0.25 was up to a value of 0.12 in a limited number of scenarios. This trend is in

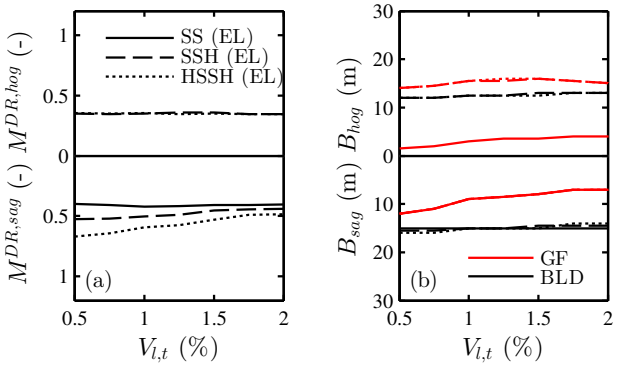

Fig. 11. Effects of the structure portion in the hogging zone on sagging deformations.

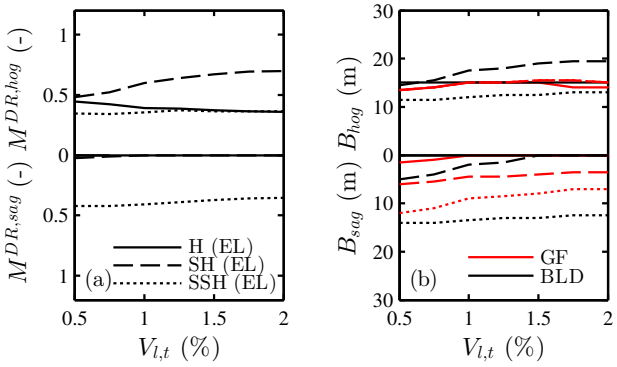

Fig. 12. Effects of the structure portion in the sagging zone on hogging deformations.

agreement with the fact that the subgrade modulus for an infinite beam on Winkler soil (Vesic, 1961) increases by 25% between $\nu_s = 0.25$ and 0.5; a variation of soil stiffness by 25% in the semi-log scale of $M^{DR} - \rho$ charts has a minor impact. Thus, in the following, $\nu_s = 0.5$ was assumed.

The following procedure was implemented to calculate the modification factors. Given the greenfield soil settlement profiles, the structure vertical displacement profile was calculated using the continuum solution proposed herein. Subsequently, the sagging and hogging zones of both the curves were defined as the regions extending between the inflection points (of the given curve) and/or the end of the structure; then, $M^{DR,sag}$, $B_{sag,gf}$, and $B_{sag,bld}$ were computed for the sagging zone above the tunnel, and $M^{DR,hog}$, $B_{hog,gf}$, and $B_{hog,bld}$ were computed for the sub-portion of the structure within the hogging zone with the maximum $DR^{hog}/DR^{hog,bld}$. In other words, for hogging, a numerical procedure was used to calculate $DR_{hog}/DR_{hog,bld}$ for all possible sub-portions of the hogging zone, and the maximum value was selected.

This approach does not require the a priori definition of cut-off distances for the settlement curves (e.g. Mair *et al.* (1996) suggested to limit the structure transverse length to where the greenfield settlement is above 1mm). Also, note that for a standard Gaussian curve and an infinite structure, the maximum $DR^{hog,gf}$ occurs when the ends of the hogging portion of the structure are assumed to be at $x = i$ and $\approx 3.7i$. This implies that, for long structures, the greenfield $B_{hog,gf} \leq 2.7i$.

Table 4. Bending stiffness for the parametric study.

Simple Beam - 15 cases	min	max
EI^* (kNm^2/m)	10^2	10^9

Firstly, the relationship between M^{DR} and both ρ and R are investigated for structures entirely located in greenfield sagging and hogging zones. Results are displayed in Figure 13 for greenfield $i = 5; 10$m, soil stiffness $E_s = 8; 80$MPa, and structures in either pure sagging ($D_l/i = -1$, $D_u/i = 1$) or pure hogging ($D_l/i = 1$, $D_u/i = 2.5$). Figure 13(a) shows agreement between the $M^{DR} - \rho$ data and the Mair (2013) envelopes, illustrating the suitability of the proposed EL analysis method to investigate the modification factors. Interestingly, both purely sagging and hogging structures are associated with the same $M^{DR} - \rho$ trend. A similar relationship between $M^{DR,sag}$ and ρ was achieved for purely sagging structures by Basmaji *et al.* (2017). Finally, results in Figure 13(b) confirm the appropriateness of the adopted dimensionless groups in Equation (15).

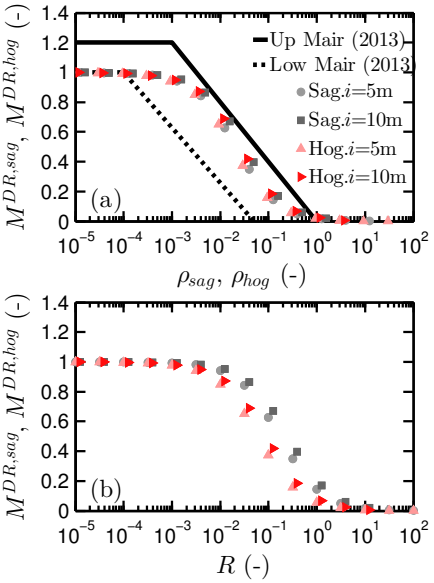

Fig. 13. M^{DR} **against (a)** ρ **and (b)** R **for structures entirely in sagging or hogging.**

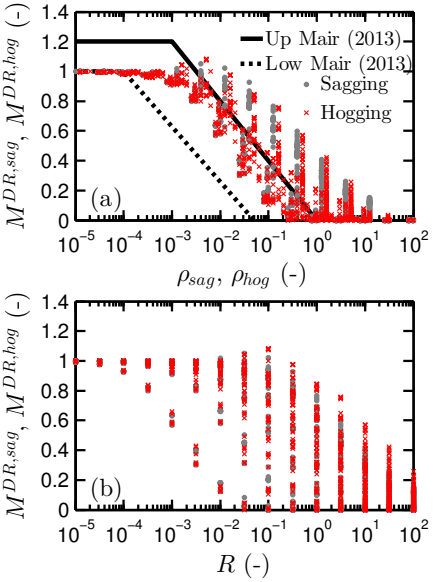

Fig. 14. Parametric study: M^{DR} **against (a)** ρ **and (b)** R**.**

Next, M^{DR} of structures spanning both sagging and hogging zones is addressed with a parametric investigation for the intervals $D_l/i = [-D_u/i, +2]$ and $D_u/i = [0.5, 10]$ (i.e. the entire range of possible structure locations) adopting $i = 5$m and $E_s = 80$MPa. This set of analyses is referred to as the 'parametric study' in the following.

For this parametric study, the trends in Figure 14(a) agree with the design curves of Mair (2013); however, there is a wide range of possible M^{DR} corresponding to the interval $\rho = [10^{-2}, 10^{1}]$. Furthermore, Figure 14(b) indicates that for a given rigidity factor R the variability of M^{DR} is also substantial.

Based on the concept that relative structure-soil stiffness could be defined with respect to the actual transverse length of the structure B_r in the sagging and hogging zones (rather than for the greenfield lengths $B_{sag,gf}$ and $B_{hog,gf}$), modified relative stiff factors ρ'_{sag} and ρ'_{hog} are defined as

$$\rho'_{sag/hog} = \frac{EI^*}{E_s B^3_{sag/hog,bld}} = \frac{\rho_{sag/hog}}{(M^{B,sag/hog})^3} \tag{16}$$

M^{DR} against ρ' are plotted for the entire parametric study in Figure 15. By adopting ρ' rather than ρ, results are confined in a narrower region of the chart (compare Figures 14(a) and 15). Additionally, an excellent agreement is obtained between

$M^{DR} - \rho'$ in Figures 13(a) and 15 (for Figure 13(a), $M^{B,sag} = M^{B,hog} = 1$ and $\rho_{sag/hog} = \rho'_{sag/hog}$). Despite the efficiency of Equation (16), there is limited guidance for the estimation of $M^{B,sag}$ and $M^{B,hog}$, which is discussed in the following.

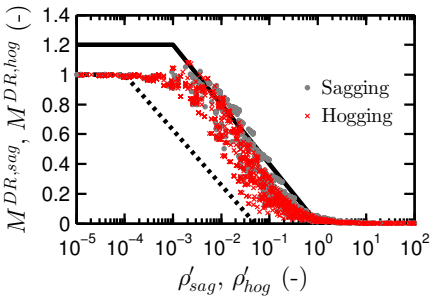

Fig. 15. Parametric study: M^{DR} against ρ'.

To distinguish between short and long structures either located in purely sagging/hogging or mixed zones, M^{DR} and M^{B} of the parametric study are plotted (lines) against R in Figures 16 and 17 for all combination of D_u/i =[1; 2; 3; 4; 7; 10] and D_l/i =[$-D_u/i$; -1; -0.5; 0; 0.5; 1]. The parametric study results (lines) are plotted in the form of design charts. For validation purposes, they are displayed along with benchmark values (markers) derived from centrifuge tests, numerical simulation and field monitoring of tunnelling in clays and sands (Dimmock & Mair, 2008; Farrell *et al.*, 2014; Franzius *et al.*, 2006; Haji *et al.*, 2018; Lu *et al.*, 2001; Mair & Taylor, 2001; Potts & Addenbrooke, 1997; Ritter *et al.*, 2017b; Taylor & Grant, 1998; Viggiani & Standing, 2001). Benchmark data are coloured according to the closest available combination of [D_u/i, D_l/i] in the plots. χ values were computed for centrifuge data based on the model structure and they were estimated for field case studies based on the available information. From each centrifuge test, several data points were defined for varying $V_{l,t}$. In particular, for a given tunnelling scenario in sand, the structure could be associated with different D_u/i and D_l/i values because of the decrease of i with tunnel volume loss. In addition, soil stiffness degradation with tunnel volume loss (i.e. E_s-$V_{l,t}$) was considered for the datasets of Farrell *et al.* (2014) and Ritter *et al.* (2017b).

In Figure 16, there is a satisfactory agreement in terms of M^{DR} between design curves and validation data for semi-flexible structures in the range $R = [10^{-2}, 10^{2}]$, whereas there is an underestimation of the deformations of fully-flexible structures with $M^{DR} > 1$ for $R < 10^{-2}$. In particular, Figures 16(a)-(f) display that, for a given D_u/i, the closer D_l/i is to D_u/i, the lower $M^{DR,sag}$. In addition, for a central structure ($e/B = 0$, $D_l/i = -D_u/i$, black solid lines) there is a variation of $M^{DR,sag}$ with D_u/i, whereas the influence of D_u/i on $M^{DR,sag}$ is limited for eccentric structures with $D_l/i = -1; -0.5; 0; 0.5$.

In Figures 16(g)-(m), $M^{DR,hog}$ curves shift towards greater rigidity factor R with the increase in D_u/i, whereas the slope of the curve in the transition zone (where an increase in R induced a decrease in $M^{DR,hog}$) reduces with D_u/i. Regarding the influence of D_l/i on $M^{DR,hog}$, it is minor except for long structures with $e/B \approx 0.5$ ($D_u/i = 4 - 10$ and $D_l/i = 0; 0.5$), for which $M^{DR,hog}$ tends to be slightly larger for $R > 10^{-2}$ prior to the transition zone (see Figures 16(i)-(m)). This indicates that structures that are predominantly in the hogging region but extend up to halfway across the sagging region deform more than similar structures in pure hogging or that extend across the entire sagging region.

Next, the predictions of $M^{B,sag}$ and $M^{B,hog}$ are addressed. In Figures 17(a)-(f), $M^{B,sag}$ increases and decreases with R for central structures and eccentric structures, respectively; however, these trends of variation were highly dependent on D_u/i. In Figures 17(g)-(m), for relatively short structures ($D_u/i \leq 4$), $M^{B,hog}$ variation is limited for eccentric structures ($D_l/i = -0.5; 0; 0.5$), whereas this modification factor decreases with R for structures centrally located above the tunnel ($D_l/i = -D_u/i$). For relatively long structures ($D_u/i \geq 7$), $M^{B,hog}$ increases within $R = [10^{-2}, 10^{1}]$ for all structure geometries; then, for further increase in $R > 10^{1}$, $M^{B,hog}$ increase and decreases, respectively, in the case of eccentric and central structures. There is fair agreement between the EL solution predictions and benchmark data, except for Ritter *et al.* (2017a) centrifuge dataset of eccentric buildings (see Figure 17(d)). This difference between the EL solution and Ritter *et al.* (2017a) data can be due to the influence of the openings (resulting in the structure deflection due to shear deformations). In fact, M^{B} may be estimated with curves in Figure 17 for structures deforming in bending; however, for structures with a pure shear deformation mode, Potts & Addenbrooke (1997) analyses suggested that $M^{B} = 1$ regardless of EI. Further studies are needed to address shear deformability effects on M^{B}.

The outcomes of the parametric study relating M^{DR} and M^{B} values to R, D_u/i, and D_l/i are given in tabular form in the supplemental data. These tables can be used in engineering practice. To approximately consider the effects of weight,

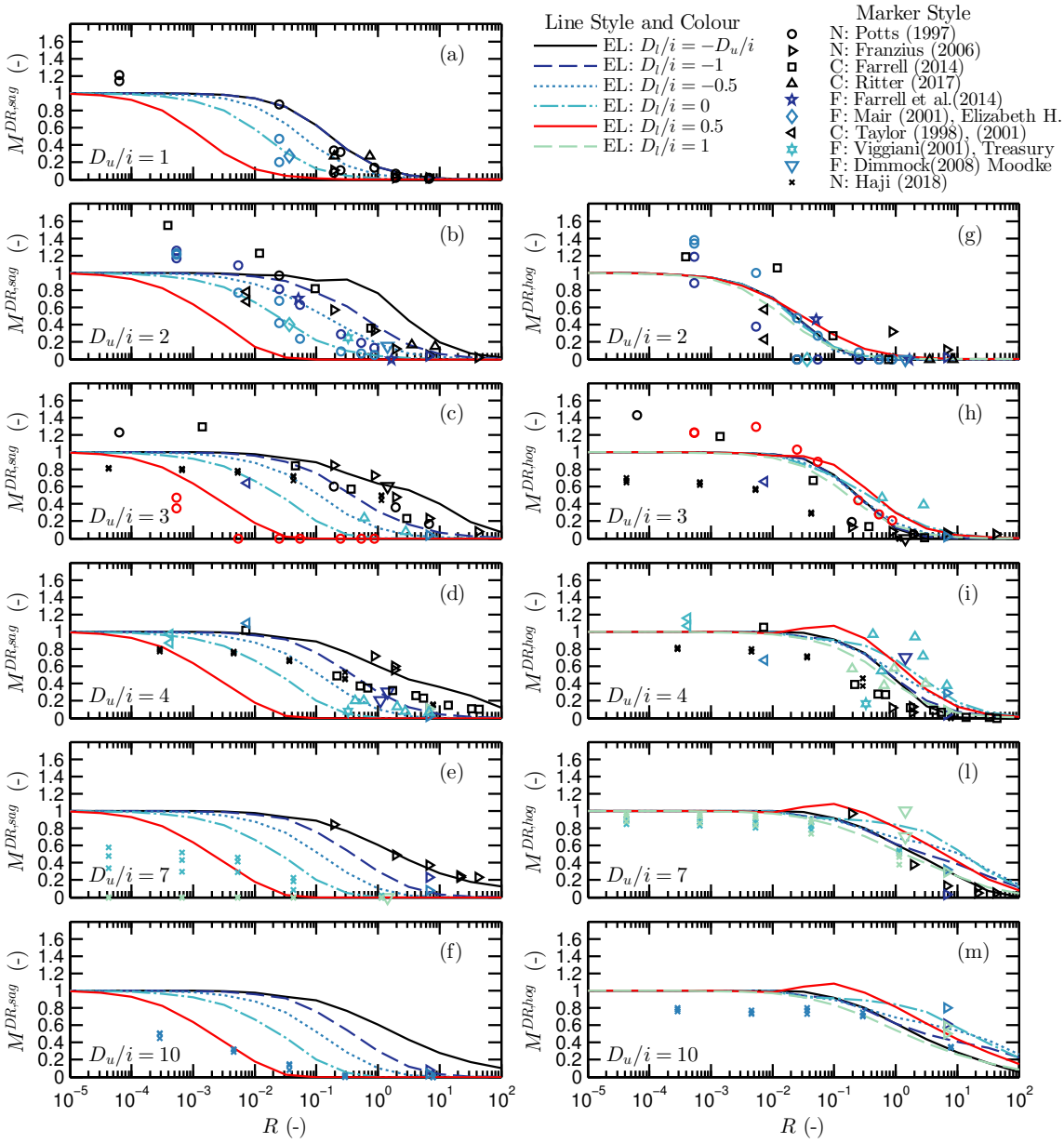

Fig. 16. Design curves of M^{DR} against R and comparison with centrifuge (C), numerical (N) and field (F) data.

for design purposes M^{DR} could be estimated as follows

$$M^{DR,design} = c^W M^{DR,cs}; \quad c^W = 1.2 - 1.4 \tag{17}$$

where $M^{DR,design}$ is the design value, and $M^{DR,cs}$ is obtained from the continuum solution. To summarise, the structure DR and B_r to be used in Equation (8) can be approximately estimated from the design charts for M^{DR} and M^B (see Figures 15, 16, and 17) while considering Equation (17) and greenfield movements.

CONCLUSIONS

Continuum solutions implementing equivalent simple beam model were used to predict tunnelling-induced deformations of structures. The following conclusions are drawn:

1. Equivalent stiffness EI^* and EA^* per meter run allowed accounting for openings as well as the foundation scheme through Melis & Rodriguez Ortiz (2001) reduction term (α) and two newly defined factors (χ and λ).

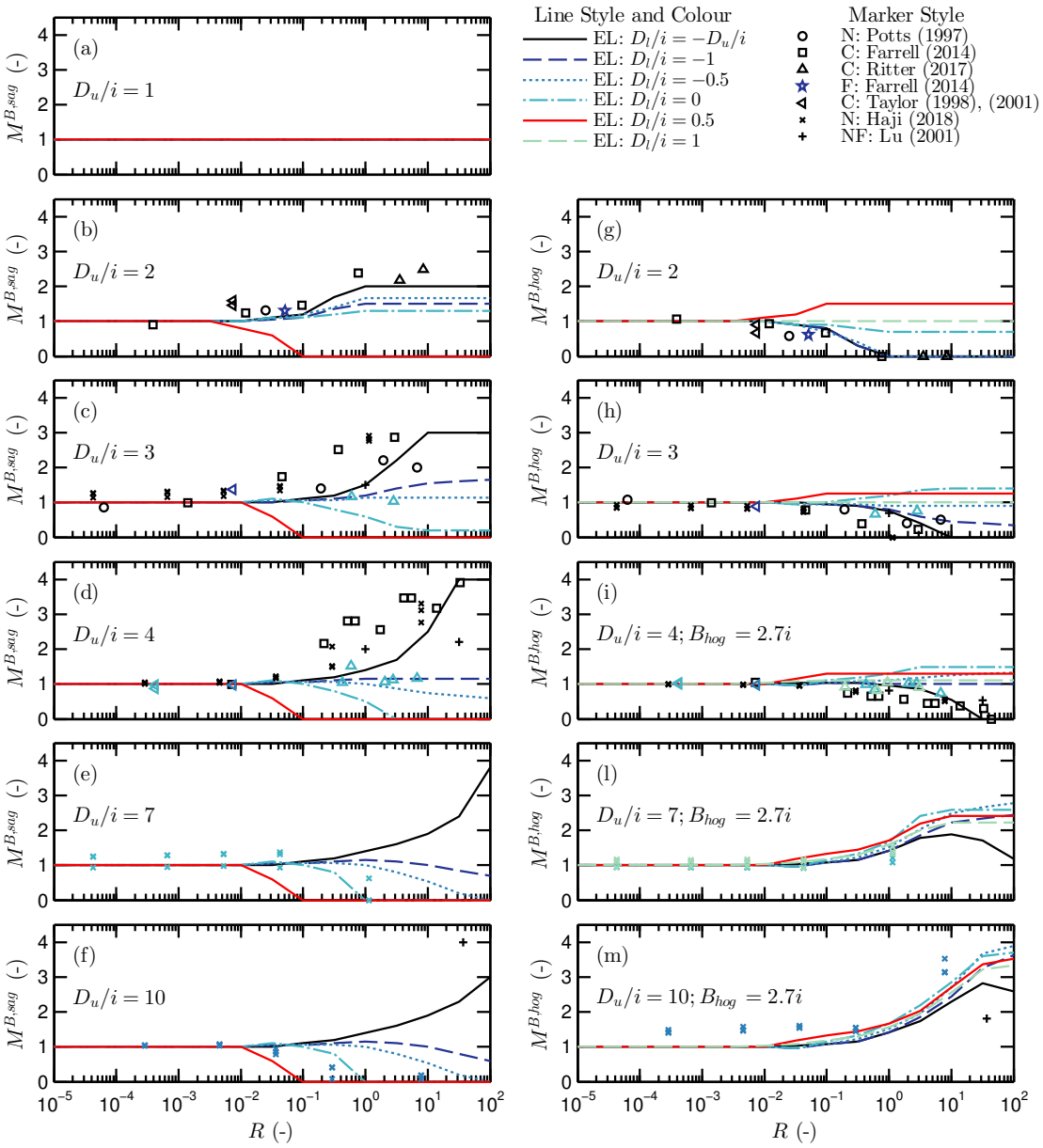

Fig. 17. Design curves of M^B against R and comparison with centrifuge (C), numerical (N) and field (F) data.

2. For structures spanning across greenfield sagging and hogging regions, the locations of the inflection points of the structure, i_{bld}, and the greenfield settlement curve, i, differed because of the continuity of semi-flexible simple beams. This interaction mechanism varied for low and high values of tunnel-structure eccentricity. Further work is needed to assess the influence of the structural shear deformability.

3. For a given structure, flexural tunnel-structure interaction depends on the width of the greenfield settlement trough, which is related to i. A modified framework was proposed to assess modification factors of deflection ratios (M^{DR}) as well as building transverse lengths (M^B) in sagging/hogging zones. The design charts and the tabular results from the parametric analysis provide a means to implement the proposed framework in practice.

ACKNOWLEDGEMENTS

This work was supported by the Engineering and Physical Sciences Research Council (EPSRC) [EP/K018221/1, EP/N509620/1] and Crossrail. The authors are grateful to Dr. S. Acikgoz and Prof. R.J. Mair for valuable comments and to Dr R.P. Farrell for sharing experimental data. The associated research data and design charts are available at [link will be provided in the final version].

NOTATION

a	parameter of the modified Gaussian curve
$b_{b,m}$	equivalent beam cross-sectional width
$d_{b,m}$	equivalent beam cross-sectional depth
c^w	weight coefficient
e	building eccentricity
g	gravity
i	distance between the centreline and the greenfield inflection point
i_{bld}	distance between the centreline and the inflection point of the building settlement trough
i_x	distance between the centreline and maximum horizontal displacement
n	shape factor used in modified Gaussian curve
$q_{z,m}$	simple beam load
t	distance between the neutral axis and the edge of the beam in tension
u_x	horizontal movement
u_z	vertical movement
$u_{x,max}$	maximum horizontal displacement
$u_{z,max}$	maximum vertical displacement
x	horizontal offset distance from tunnel centreline
z	depth, measured from ground surface
z_b	neutral axis level for pure bending deformations
z_g	ground level
z_t	depth of tunnel axis
A	cross-sectional area
A_m	cross-sectional area of the equivalent beam model
A_f	contact area of the foundation
A_s	contact area of the building
B	building transverse length
B_r	building length in the sagging or hogging region
$B_{sag/hog,bld}$	transverse length of the sagging/hogging region of the building settlement trough
$B_{sag/hog,gf}$	transverse length of the sagging/hogging region of the greenfield settlement trough
C	cover: distance from surface to tunnel crown
D	tunnel diameter
D_l	minimum offset of the structure edges from the tunnel centreline
D_u	maximum offset of the structure edges from the tunnel centreline
$DR_{sag/hog,bld}$	deflection ratio in the sagging/hogging region of the building settlement trough
$DR_{sag/hog,gf}$	deflection ratio in the sagging/hogging region of the greenfield settlement trough
E	Young's modulus of the structure
E_m	Young's modulus of the equivalent beam model
E_s	Young's modulus of the soil
EA	axial stiffness
EA^*	axial stiffness per m run
EI	bending stiffness
EI^*	bending stiffness per m run
G	shear modulus
H	building height
I	second moment of area
I_m	second moment of area of the equivalent beam model
I_d	relative density
L	building longitudianl length
M^B	modification factor for the sagging and hogging region length
M^{DR}	modification factor for the deflection ratio
N	centrifuge acceleration
O	ratio of façade openings
R	rigidity factor
$V_{l,s}$	volume loss of soil
$V_{l,t}$	volume loss of tunnel

EL	elastic solution
EP	elastoplastic solution
EXP	experimental
SLD	slider
STR	structure/building
α	bending stiffness reduction factor
χ	ratio between foundation and building areas
λ	axial stiffness reduction factor
μ	friction coefficient
ν_s	Poisson's ratio of the soil
$\rho_{sag/hog}$	relative structure-soil stiffness defined with respect to i
$\rho'_{sag/hog}$	relative structure-soil stiffness defined with respect to i_{bld}
ρ^*_{mod}	relative structure-soil stiffness
σ	contact stress between foundation and soil
ε_h	horizontal strain
$\varepsilon_{h,sag/hog,bld}$	horizontal strain in the sagging/hogging region of the building settlement trough
$\varepsilon_{h,sag/hog,gf}$	horizontal strain in the sagging/hogging region of the greenfield settlement trough

REFERENCES

Basmaji, B., Deck, O. & Al Heib, M. (2017). Analytical model to predict building deflections induced by ground movements. *European Journal of Environmental and Civil Engineering* , 1–23doi:10.1080/19648189.2017.1282382.

Bilotta, E., Paolillo, A., Russo, G. & Aversa, S. (2017). Displacements induced by tunnelling under a historical building. *Tunnelling and Underground Space Technology* **61**, 221–232, doi:10.1016/j.tust.2016.10.007.

Boscardin, M. D. & Cording, E. J. (1989). Building response to excavation-induced settlement. *Journal of Geotechnical Engineering* **115**, No. 1, 1–21.

Burd, H. J., Houlsby, G. T., Augarde, C. E. & Liu, G. (2000). Modelling tunnelling-induced settlement of masonry buildings. *Proceedings of the Institution of Civil Engineers-Geotechnical Engineering* **143**, No. 1, 17–29.

Burland, J. B., Mair, R. J. & Standing, J. R. (2004). Ground performance and building response due to tunnelling. In *Advances in Geotechnical Engineering: The Skempton Conference - Proceedings of a Three Day Conference on Advances in Geotechnical Engineering, organised by the Institution of Civil Engineers*, vol. 1 (Jardine, R. J., Potts, D. M. & Higgins, K. G., eds.), London, United kingdom: Thomas Telford Services Ltd, pp. 291–344.

Burland, J. B. & Wroth, C. P. (1974). Settlement of buildings and associated damage. In *Proceedings of the conference on settlement of structures*, London, UK: Pentech Press, pp. 611–654.

Dimmock, P. S. & Mair, R. J. (2008). Effect of building stiffness on tunnelling-induced ground movement. *Tunnelling and Underground Space Technology* **23**, No. 4, 438–450, doi:10.1016/j.tust.2007.08.001.

Fargnoli, V., Gragnano, C. G., Boldini, D. & Amorosi, A. (2015). 3D numerical modelling of soilâĂŞstructure interaction during EPB tunnelling. *Géotechnique* **65**, No. 1, 23–37, doi:10.1680/geot.14.P.091.

Farrell, R. (2010). Tunnelling in sands and the response of buildings. *Ph.D. Thesis, Cambridge University* .

Farrell, R., Mair, R., Sciotti, A. & Pigorini, A. (2014). Building response to tunnelling. *Soils and Foundations* **54**, No. 3, 269–279, doi:10.1016/j.sandf.2014.04.003.

Franza, A. & DeJong, M. J. (2018). Elastoplastic solutions to predict tunnelling-induced load transfer and deformation mechanisms of surface structures. *Journal of Geotechnical and Geoenvironmental Engineering (In Press)* doi:10.1061/(ASCE)GT.1943-5606.0002021.

Franza, A. & Marshall, A. M. (2018). Centrifuge Modeling Study of the Response of Piled Structures to Tunneling. *Journal of Geotechnical and Geoenvironmental Engineering* **144**, No. 2, 04017109, doi:10.1061/(ASCE)GT.1943-5606.0001751.

Franza, A., Marshall, A. M., Haji, T., Abdelatif, A. O., Carbonari, S. & Morici, M. (2017). A simplified elastic analysis of tunnel-piled structure interaction. *Tunnelling and Underground Space Technology* **61**, No. January, 104–121, doi:10.1016/j.tust.2016.09.008.

Franza, A., Marshall, A. M. & Zhou, B. (2018). Greenfield tunnelling in sands: the effects of soil density and relative depth. *Géotechnique (In press)* doi:10.1680/jgeot.17.p.091.

Franzius, J. N., Potts, D. M., Addenbrooke, T. I. & Burland, J. B. (2004). The influence of building weight on tunnelling-induced ground and building deformation. *Soils and Foundations* **44**, No. 1, 25–38.

Franzius, J. N., Potts, D. M. & Burland, J. B. (2006). The response of surface structures to tunnel construction. *Proceedings of the ICE - Geotechnical Engineering* **159**, No. 1, 3–17, doi:10.1680/geng.2006.159.1.3.

Frischmann, W., Hellings, J., Gittoes, G. & Snowden, C. (1994). Protection of the Mansion House against damage caused by ground movements due to the Docklands Light Railway Extension. *Proceedings of the Institution of Civil Engineers - Geotechnical Engineering* **107**, No. 2, 65–76, doi:10.1680/igeng.1994.26374.

Giardina, G., DeJong, M. J. & Mair, R. J. (2015). Interaction between surface structures and tunnelling in sand: Centrifuge and computational modelling. *Tunnelling and Underground Space Technology* **50**, 465–478, doi:10.1016/j.tust.2015.07.016.

Haji, T. K., Marshall, A. M. & Franza, A. (2018). Mixed empirical-numerical method for investigating tunnelling effects on structures. *Tunnelling and Underground Space Technology* **73**, 92–104, doi:10.1016/j.tust.2017.12.008.

Klar, A., Vorster, T. E. B., Soga, K. & Mair, R. J. (2005). Soil-pipe interaction due to tunnelling : comparison between Winkler and elastic continuum solutions. *Géotechnique* **55**, No. 6, 461–466.

Losacco, N., Burghignoli, A. & Callisto, L. (2014). Uncoupled evaluation of the structural damage induced by tunnelling. *Géotechnique* **64**, No. 8, 646–656, doi:10.1680/geot.13.P.213.

Lu, Y.-C., Bloodworth, A. G. & Gleig, F. D. (2001). Behaviour of long structures in response to tunnelling. In *Proceedings of the international conference Response of buildings to excavation-induced ground movements* (Jardine, F. M., ed.), London, UK: CIRIA, pp. 367–374.

Mair, R. (2013). Tunnelling and deep excavations: ground movements and their effects. In *Proceedings of the 15th European Conference on Soil Mechanics and Geotechnical Engineering - Geotechnics of Hard Soils - Weak Rocks (Part 4)* (Anagnostopoulos, A., Pachakis, M. & Tsatsanifos, C., eds.), Amsterdam, the Netherlands: IOS Press, pp. 39 – 70.

Mair, R. J. & Taylor, R. N. (2001). Elizabeth House: settlement predictions. In *Building response to tunnelling: case studies from the Jubilee Line Extension, London. Volume 1: Projects and Methods* (Burland, J. B., Standing, J. R. & Jardine, F. M., eds.), London, United Kingdom: CIRIA and Thomas Telford, pp. 195–215.

Mair, R. J., Taylor, R. N. & Bracegirdle, A. (1993). Subsurface settlement profiles above tunnels in clay. *Géotechnique* **43**, No. 2, 315–320, doi:10.1680/geot.1993.43.2.315.

Mair, R. J., Taylor, R. N. & Burland, J. B. (1996). Prediction of ground movements and assessment of risk of building damage due to bored tunnelling. In *Proceedings of the International Symposium on Geotechnical Aspects of Underground Construction in Soft Ground* (Mair, R. J. & Taylor, R. N., eds.), London, United Kingdom: Balkema, Rotterdam, pp. 713–718.

Marshall, A. M., Farrell, R., Klar, A. & Mair, R. (2012). Tunnels in sands: the effect of size, depth and volume loss on greenfield displacements. *Géotechnique* **62**, No. 5, 385–399, doi:10.1680/geot.10.P.047.

Melis, M. J. & Rodriguez Ortiz, J. M. (2001). Consideration of the stiffness of buildings in the estimation of subsidence damage by EPB tunnelling in the Madrid subway. In *Proceedings of international conference: response of buildings to excavation induced ground movements, London*, London, UK: Ciria Special Publication 201, pp. 87–394.

Namazi, E. & Mohamad, H. (2013a). Assessment of Building Damage Induced by Three-Dimensional Ground Movements. *Journal of Geotechnical and Geoenvironmental Engineering* **139**, No. 4, 608–618, doi:10.1061/(ASCE)GT.1943-5606.0000822.

Namazi, E. & Mohamad, H. (2013b). Potential damage assessment in buildings undergoing tilt. *Proceedings of the Institution of Civil Engineers-Geotechnical Engineering* **166**, No. 4, 365–375, doi:10.1680/geng.10.00132.

Peck, R. B. (1969). Deep excavations and tunnelling in soft ground. In *Proceedings of the 7th International Conference on Soil Mechanics and Foundation Engineering*, Mexico City, Mexico, pp. 225–290.

Pickhaver, J., Burd, H. & Houlsby, G. (2010). An equivalent beam method to model masonry buildings in 3D finite element analysis. *Computers & Structures* **88**, No. 19, 1049–1063, doi:10.1016/j.compstruc.2010.05.006.

Potts, D. M. & Addenbrooke, T. I. (1997). A structure's influence on tunnelling-induced ground movements. *Proceedings of the ICE - Geotechnical Engineering* **125**, No. 2, 109–125.

Ritter, S. (2017). Experiments in tunnel-soil-structure interaction. *Ph.D. thesis, University of Cambridge* doi:10.17863/CAM.20966.

Ritter, S., Giardina, G., DeJong, M. J. & Mair, R. J. (2017a). Centrifuge modelling of building response to tunnel excavation. *International Journal of Physical Modelling in Geotechnics* doi:10.1680/jphmg.16.00053.

Ritter, S., Giardina, G., DeJong, M. J. & Mair, R. J. (2017b). Influence of building characteristics on tunnelling-induced ground movements. *Géotechnique* **67**, No. 10, 926–937, doi:10.1680/jgeot.SIP17.P.138.

Sugiyama, T., Hagiwara, T., Nomoto, T., Nomoto, M., Ano, Y., Mair, R., Bolton, M. & Soga, K. (1999). Observations of ground movements during tunnel construction by slurry shield method at the Docklands Light Railway Lewisham Extension-East London. *Soils and Foundations* **39**, No. 3, 99–112.

Taylor, R. N. & Grant, R. J. (1998). Centrifuge modelling of the influence of surface structures on tunnelling induced ground movements. In *Tunnels and Metropolises*, pp. 261–266.

Taylor, R. N. & Yip, D. L.-F. (2001). Centrifuge modelling of the effect of a structure on tunnel-induced ground movements. In *Proceedings of the International Conference on the response of buildings to excavation-induced ground movements* (Jardine, F. M., ed.), London, UK: CIRIA, pp. 601–611.

Vaziri, H., Simpson, B., Pappin, J. W. & Simpson, L. (1982). Integrated forms of Mindlin's equations. *Géotechnique* **32**, No. 3, 275–278.

Vesic, A. B. (1961). Bending of beams resting on isotropic elastic solid. *Journal of the Engineering Mechanics Division* **87**, No. EM2, Part 1, 35–53.

Viggiani, G. & Standing, J. (2001). The Treasury. In *Building response to tunnelling: case studies from the Jubilee Line Extension, London. Volume 2: Case studies* (Burland, J. B., Standing, J. R. & Jardine, F. M., eds.), CIRIA and Thomas Telford, pp. 401–423.

Vorster, T. E. B., Klar, A., Soga, K. & Mair, R. J. (2005). Estimating the Effects of Tunneling on Existing Pipelines. *Journal of Geotechnical and Geoenviromental Engineering* **131**, No. 11, 1399–1410, doi:10.1061/(ASCE)1090-0241(2005)131:11(1399).